*Arab J. Nucl. Sci. Appl., Vol. 55, 4, 16-28 (2022)*

ISSN 1110-0451

**Arab Journal of Nuclear Sciences and Applications**

**Web site: ajnsa.journals.ekb.eg**

(E S N S A)

# Effect of Methyl Cellulose "MC" on some Physical Properties of Nickel Magnesium Ferrite - MC Nanocomposite

**M. Mostafa[1*], O. Saleh[1], M. El-Shahawy[1], R. Ghazy[1], O.M. Hemeda[1], S. A. Abd El-Kareem[2], A. M. Dorgham[3]**

*(1)Physics Department, Faculty of Science, Tanta University, Egypt*

*(2) Medical Research Institute, Alexandria University, Egypt*

*(3) Basic Science Department , Higher Institute of Engineering andTechnology, Shopra Elnamla, Tanta, Egypt*

ARTICLE INFO

*Article history:*

Received: 29th Dec. 2021.

Accepted: 14th June 2022.

*Keywords:*

XRD,
FTIR,
HRTEM,
SEM,
TGA,
Permeability,
Methyl Cellulose.

ABSTRACT

**$Ni_{0.6}Mg_{0.4}Fe_2O_4$ ferrite sample was obtained employing the auto combustion flash technique and is overheated for three hours at 700℃. Utilizing the casting procedure, a freestanding magnetic film was created by combining $Ni_{0.6}Mg_{0.4}Fe_2O_4$ nanoparticles with methyl cellulose (MC). X-ray Diffraction (XRD), transmission electron microscopy (TEM), and Fourier transition infrared spectroscopy (FTIR) are hired to depict the structural properties of the synthesized samples. All samples' surface morphology was tutored employing scanning electron microscopy (SEM). M-H loops were harnessed to mensuration magnetic properties such as coercivity (Hc), saturation magnetization (Ms), and retentivity (Mr). At various frequencies, the temperature dependence of the initial magnetic permeability was gauged. The Ultraviolet and visible spectroscopy (UV-vis) absorption spectrum displayed that the absorption of $Ni_{0.6}Mg_{0.4}$ $Fe_2O_4$ at MC is in the UV-A region up to 270 nm.**

## 1. INTRODUCTION

Semiconductor nanostructures have recently been widely hired in photovoltaic devices espicially dye sensitized and whole inorganic nanoparticles [1]. Distinct cellulose-based materials have been incubated and utilized as sorbents or photocatalysts in the removal of watery pollutants on account of cellulose's natural abundance, low cost, renewability, and sustainability [1–6]. Raw cellulose, on the other hand, possesses a faint surface area, indigent interaction for pollutants, fading solubility, and reusing issues. Ethers, esters, and ionic functionalizations have been developed to address those snags, and bonding of cellulose and nanomaterials for the production of advanced cellulose derivatives [7]. The combination of MC with magnetic nanoparticles resulted in a biomagnetic catalyst that was particularly effective in photodegrading organic contaminants in wastewater [9–11]. Furthermore, MC is a non-toxic, biodegradable, antioxidant, and filmable carbohydrate polymer [12]. To remove pollutants from wastewater and water and affect its biophysical and chemical properties, many functionalized and magnetized derivatives of MC have been developed [13]. At the oxygen atoms of MC, there are non-bonding electron pairs that can act as complexation sites for the cation salt [14]. Polymer nanocomposites have received a lot of attention in the last two decades, jointly in terms of science and technology [15]. Polymer nanocomposites, including semiconductor nanoparticles, have been demonstrated to be useful in the fabrication of electronic and optoelectronic components such as solar cells, LEDs, optical limiters, and distinct kinds of sensors [16]. Many material scientists are interested in the manufacture and evolution of polymer instituted nanocomposites toward potential enforcements in technology [17]. In spite of the disadvantages for hiring inorganic nano materiality could mitigate with embedding a teeny amount of inorganic nanoparticles on a polymer form [15]. A semiconductor substance with adequate bandgap around 1 eV could be the farthest difficult aspects of photovoltaic and optoelectronics [18]. Grasping the relevance among nanocomposite optical merits and structural features is directly related to the technological importance of such materials. As a result, its suitability in various applications can be predicted

Corresponding author: maha_mostafa@science.tanta.edu.eg
DOI: 10.21608/ajnsa.2022.113739.1537

[19]. According to a previous study [20], the majority of conjugated polymers with intramolecular charge transfer (ICT) properties are narrow bandgap materials. Incorporating jointly donor and acceptor sort semiconductors in conjugated polymers could also be a viable strategy for producing photovoltaic devices with high external quantum efficiency [21,22]. However, conjugated polymers have a number of drawbacks, including low efficiency and rapid degradation [23]. Polar polymers, otherwise, including MC, Polyvinyl alcohol (PVA), and chitosan, are inexpensive, have a long shelf life and good filmability. The present study describes a simple and environmentally friendly method for producing freestanding magnetic films using ($NiMgFe_2O_4$) nanoparticles and methyl cellulose.

## 2. Experimental Procedure and Method

As shown in flowchart (1), a ferrite sample was manufactured from $Ni_{0.6}Mg_{0.4}Fe_2O_4$ using the flash auto combustion process [24]. Next, as shown in flowchart (2), a magnetic film based on the combination of $Ni_{0.6}Mg_{0.4}Fe_2O_4$ nanoparticles and methylcellulose was prepared using a casting method. Specimens were inspected with x-ray diffraction employing a Philips model (PW-1729) diffractometer (Cu-Kα radiation source with λ= 1.540598 Å) from 20-80° at 2Θ. The specimen microstructure is decomposed by TEM (JEOL1010) and scanning electron microscope (SEM) (JEOL JSM-6460, Japan). FTIR spectrum was performed harnessing infrared spectrometer in wavenumber scale of 200–4000 $cm^{-1}$ (Perkin-Elmer 1430, Germany). The magnetic hysteresis loops were mensuration at room temperature utilizing vibrating sample magnetometer (VSM) operating system v 1.6 control software Oxford OX8JTL, England. For all the toroidal samples, the magnetic permeability was gauged as a function of temperature. Changes in optical properties were investigated utilizing Ultraviolet-Visible (UV-Vis) spectrometer (V-630 UV-Vis) with range (190 to 1100 nm) with fixed band pass of 1.5 nm.

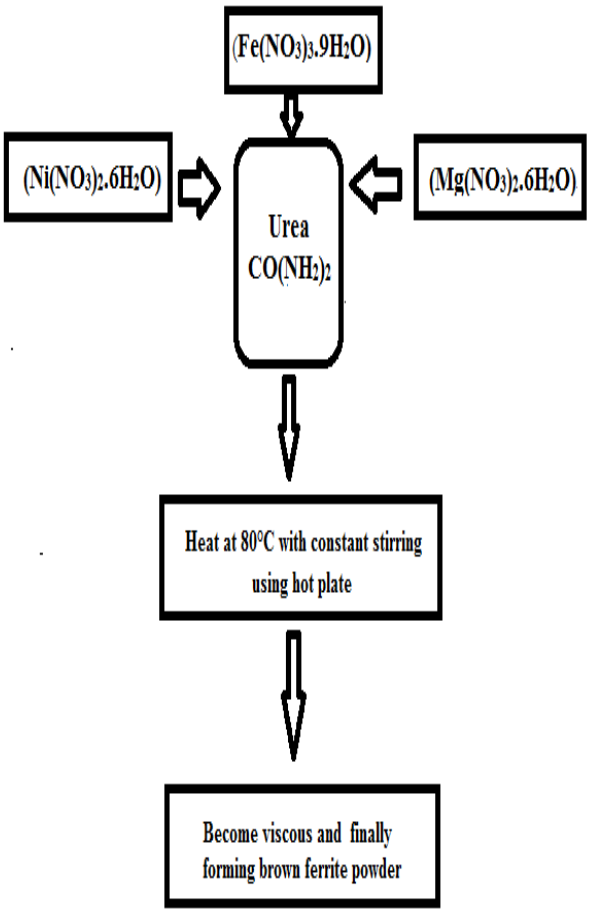


**Flowchart (1): Flash auto combustion method.**

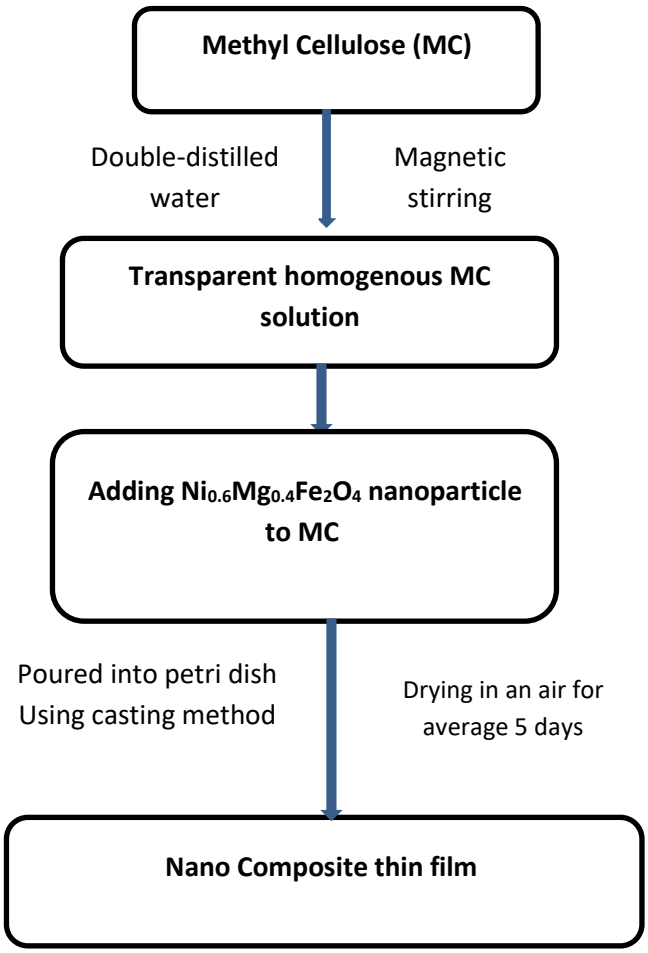


**Flowchart (2): casting method**.

## 3. RESULTS AND DISCUSSION

### 3.1. X-ray diffraction (XRD)

The XRD patterns of the $Ni_{0.6}Mg_{0.4}Fe_2O_4$ sample, which was calcined for 3 hours at 700 ° C, is presented in Fig. (1), that affirms the single cubic spinel phase. The patterns assured the polycrystalline nature which is a part of FCC Bravias lattice. The acquired worth of lattice parameter is given in Table (1). Ni and Mg are both inverse ions. The Mg ions tend to conquer both tetrahedral and octahedral site that force $Fe^{3+}$ ion to immigrate from tetrahedral to octahedral site. The worth of theoretical lattice parameter was deemed from the cation distribution as given in Table (1) utilizing formula $a_{th} = \frac{8}{3\sqrt{3}} [ (r_A + r_o) + \sqrt{3} ( r_B + r_o ) ]$ , where $r_o$ is the Oxygen ion radius $an\ dr_A$ and $r_B$ are the radii of A and B sites. The worth of $a_{th}$ agrees well with the experimentally gained value.

XRD diffractogram of MC offered the exemplary diffraction peaks of the crystalline structure of cellulose at 12.3°, 20.1°, and 21.7° symmetry (110), (102) and (200) planes, respectively. The pattern of the NiMg ferritee/MC composite was clearly various from cellulose. Furthermore, the predestine broad refection peaks of alkali cellulose could be because of the interaction of NiMg ferritee particles with MC. The diffraction peaks of NiMg ferrite were noticed with 2θ worth of 30.1°, 33.0°, 35.3°,38.0°, 41.4°, 46.5°, and 48.3° symmetry the reflexion patterns of (220), (311), (222), (400), (422), (511), and (440), respectively, refereeing the existence of a spinel cubic structure.

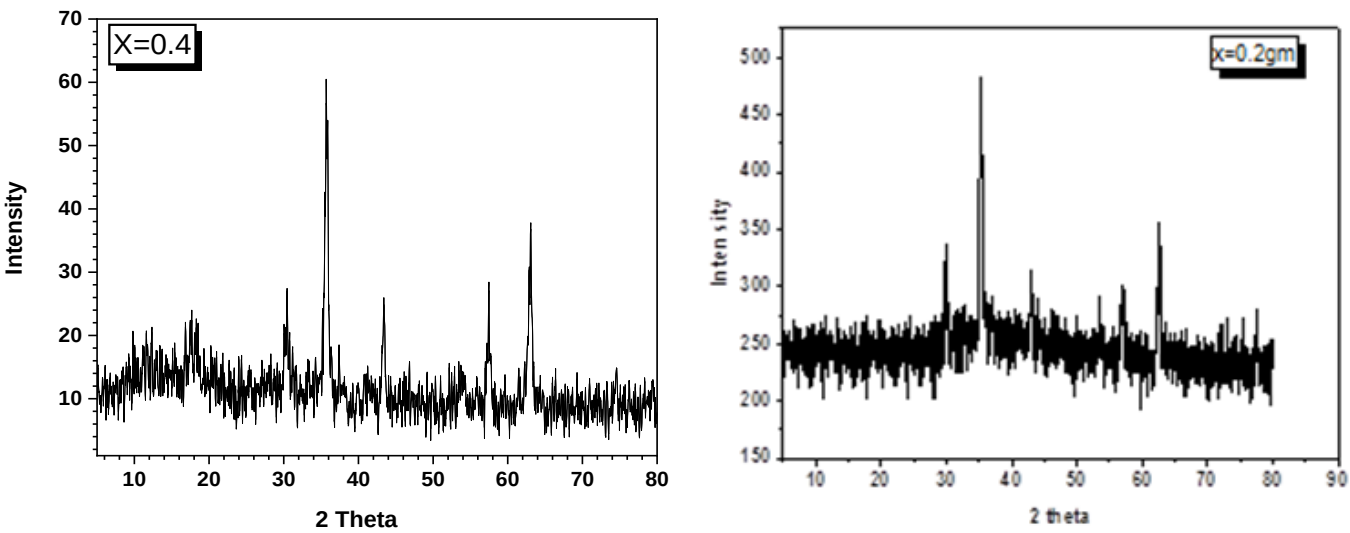


**Fig. (1): X-ray diffraction patterns of system ferrite $Ni_{0.6}Mg_{04}Fe_2O_4$ and $Ni_{0.6}Mg_{0.4}Fe_2O_4$ with methyl cellulose**

**Table (1): Experimental lattice parameters ($a_{exp}$) and theoretical lattice parameters ($a_{th}$), X-ray cation distribution, ionic radius of A-site ($r_A$),ionic radius of B-site ($r_B$), oxygen positional parameter (u), inversion parameter (δ) and bond length of A-site ($R_A$) and B-site ($R_B$) for $Ni_{0.6}Mg_{0.4}Fe_2O_4$ system**

| sample | Lattice parameter | | Cation distribution | | $r_A$ (Å) | $r_B$ (Å) | u | δ | Bond length | | $\mu_{th}$ ($\mu_B$) |
|---|---|---|---|---|---|---|---|---|---|---|---|
| | ath (Å) | aexp (Å) | A-site | B-site | | | | | $R_A$ | $R_B$ | |
| $Ni_{0.6}Mg_{04}Fe_2O_4$ | 8.327 | 8.325 | $(Mg^{+2}_{0.008}\ Fe^{+3}_{0.992})$ | $[Mg^{+2}_{0.392}\ Ni^{+2}_{0.6}\ Fe^{+3}_{1.008}]$ | 0.6406 | 0.670 | 0.3859 | 0.0109 | 1.9606 | 1.994 | 1.28 |

### 3.2. High Resolution Transmission Electron Microscopy (HRTEM)

TEM images of $Ni_{0.6}$ $Mg_{0.4}$ $Fe_2O_4$ of high resolution and electron diffraction are illustrated in Fig. (2a). The images reveals a nanocrystalline nature with several agglomeration on account of the magnetic interaction among Nano parts. The crystallites are spherical in shape and their sizes are reconciles well with that gained from XRD mensuration utilizing Sherer's formula as given in Table (2). The micrographs exhibit that the particles have size distribution about 19nm. A corresponding lattice planes appear and the predestine crystallographic worth of inter planner distance (d) equals 2.43 Å corresponding to plan (311) that assured the formation of the spinel phase of ferrite. The observed crystallographic d worth concurred with those gained from XRD dissection, so the spinel phase of ferrite is affirmed by TEM and XRD. From Fig. (2), the electron diffraction pattern consists of a group of concentric halo rings that point out the nanocrystalline nature of the samples [25]. The bright spots in the halo rings display the well crystallization of the material. The crystalline lattice planes for the various circles symmetry to various peaks are realized as (220), (311), (400), (511) and (440) that appeared at the XRD pattern that displays the significance among electron diffraction pattern and XRD pattern [25].

For affirming the interaction among $Ni_{0.6}$ $Mg_{0.4}$ $Fe_2O_4$ and MC in the composite, the micrograph of the $Ni_{0.6}$ $Mg_{0.4}$ $Fe_2O_4$ /MC was inspected with TEM. The HRTEM images of the $Ni_{0.6}$ $Mg_{0.4}$ $Fe_2O_4$ /MC are illustrated in Fig. (2b).The images proposed that the ferrite nanoparticles were successfully supported on the MC. The nanoparticles displayed spherical particles. It is obvious that the nanoparticles showed some agglomeration because of their small particle size. The electron diffraction halos intensity decrease indicates the decrease of crystallinity of composites.

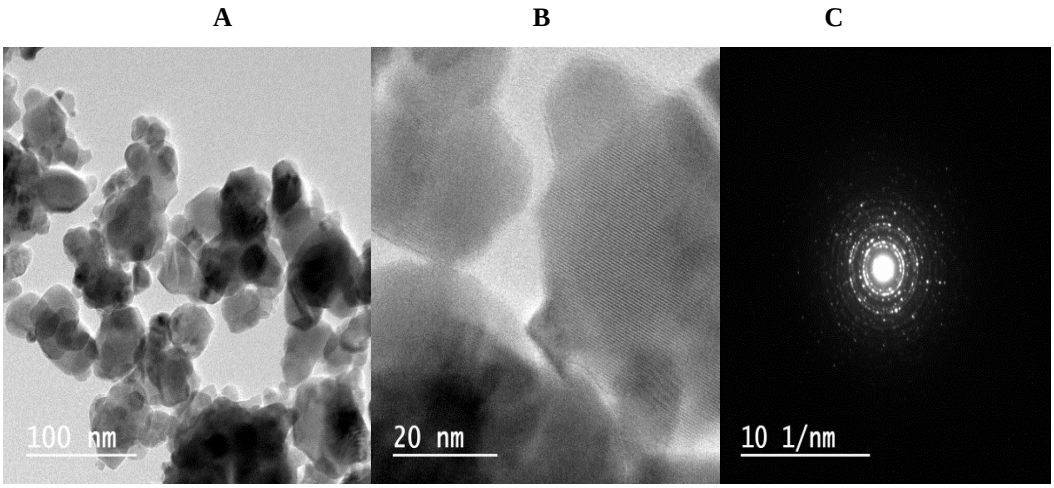


**(a)**

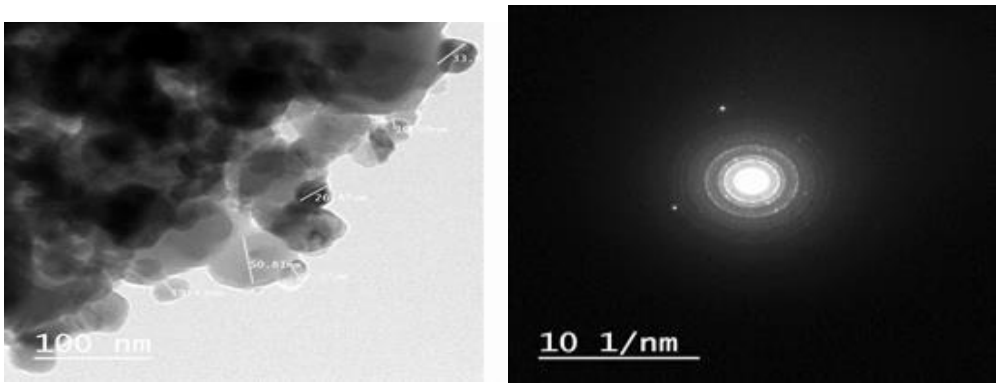


**(b)**

**Fig. (2) A: HRTEM images, B: The fringing spacing and C: selected area electron diffraction pattern and Selected area electron diffraction pattern for (a) $Ni_{0.6}Mg_{0.4}$ $Fe_2O_4$ and (b) $Ni_{0.6}Mg_{0.4}Fe_2O_4$ with methyl cellulose**

**Table (2): Crystallite size obtained from HRTEM and XRD and grain size for $Ni_{0.6}Mg_{0.4}$ $Fe_2O_4$ and $Ni_{0.6}Mg_{0.4}Fe_2O_4$ with methyl cellulose**

| Sample | Crystallite size from HRTEM (nm) | Crystallite size from XRD (nm) | SEM Grain Size (nm) |
|---|---|---|---|
| $Ni_{0.6}Mg_{0.4}$ $Fe_2O_4$ | 16.78 | 18.943 | 108.66 |
| $Ni_{0.6}Mg_{0.4}Fe_2O_4$ with MC | 28.08 | 46.58 | 79.77 |

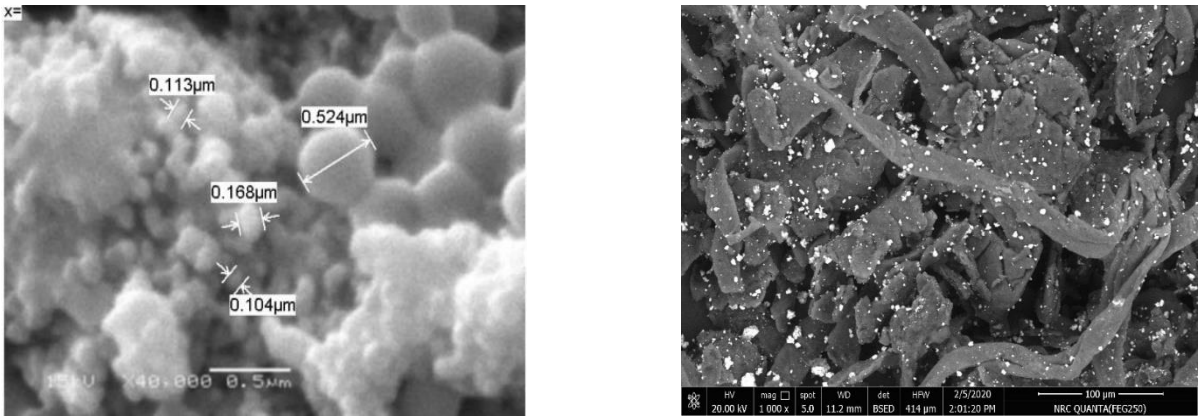


**(a)** **(b)**

**Fig. (3): SEM micrograph of (a) $Ni_{0.6}Mg_{0.4}Fe_2O_4$ and (b) $Ni_{0.6}Mg_{0.4}Fe_2O_4$ with methyl cellulose**

### 3.3 Scanning Electron Microscopy Analysis (SEM)

The morphology of the studied sample $Ni_{0.6}$ $Mg_{0.4}$ $Fe_2O_4$ was examined utilizing scanning electron microscopy as shown in Fig. (3a). The grains manifest as spherical shape with highly compact state. Average grain size was gauged utilizing the intercept manner put up with the equation [26].

$$Grain\ size = \frac{1.5\ L}{M\ N}$$

Where L is the total length of the test line, M is the magnification and N is the total number of intercepts in the micrographs. Its worth is found to be 0.10866 µm.

SEM image of MC and its ferrite composite is presented in Fig. (3b). As could be obvious from Fig.(3b), the composite surface consists of cylindrical fibers with steady ferrite grains strewn through MC fibers implicating several vacants indicating the composite's high porosity and resistivity. The vacancy has a significant impact on the composite's diametric swelling. The fiber structure also contributed to the composite's increased tensile strength (high mechanical stability).

### 3.4. FTIR studies

The FTIR spectra of the nanoferrite samples $Ni_{0.6}$ $Mg_{0.4}Fe_2O_4$ annealed at 700°C for 3hours are presented in Fig. (4). The absorption spectra exhibit two major absorption bands in the extent 579 $cm^{-1}$ and 388 $cm^{-1}$. The first one was specified to stretching vibration of $Fe^{+3}$ – $O^{-2}$ at tetrahedral site, whereas second one particular to octahedral site bond vibration [27]. The peaks round 1414 $cm^{-1}$ represent the pending vibration of O-H that are assigned to O-H absorbed by nanoparticle [27], whereas those appear nearly 3500 $cm^{-1}$ and 1600 $cm^{-1}$ could be on account of H-O-H stretching vibration mode and water molecule bending vibration [24].

Comparative FT-IR spectra of $Ni_{0.6}Mg_{0.4}Fe_2O_4$ + MC reveal absorption bands of O-H stretching within 3472.48 $cm^{-1}$, C-H stretching by >3000 $cm^{-1}$, adsorbed water stretching near 1646.91 $cm^{-1}$, C-H bending of methylene and methyl groups at 1458.17 $cm^{-1}$ and 1376.04 $cm^{-1}$, respectively, and C-O stretching at 1100-1150 $cm^{-1}$ of MC. The broad peak on 3420.81$cm^{-1}$ was on account of stretching modes of superposition OH for aliphatic C-H stretching; the peak around 1636 $cm^{-1}$ is attributed to adsorbed surface water; and the vibration mode of CH3-bending was predestined on 1384.46 $cm^{-1}$. In Ni Mg ferrite + MC, the highest band ($\upsilon_1$) was observed at 592.01 $cm^{-1}$ that of intrinsic stretching vibrations of the metal cation at the tetrahedral site. The lowest one ($\upsilon_2$) was located at 400 $cm^{-1}$ that symmetry the metal cation at the octahedral site.

Utilizing the formula $F = 4\pi^2\ C^2\ \mu\ \nu^2$ , where C: is the light velocity, $\nu$ is the wavenumber of frequency and µ is the reduced mass [28], the Force constant (F) for $Fe^{+3}$ – $O^{-2}$ bonds at jointly tetrahedral and octahedral site was estimated and tabulated in Table (3).

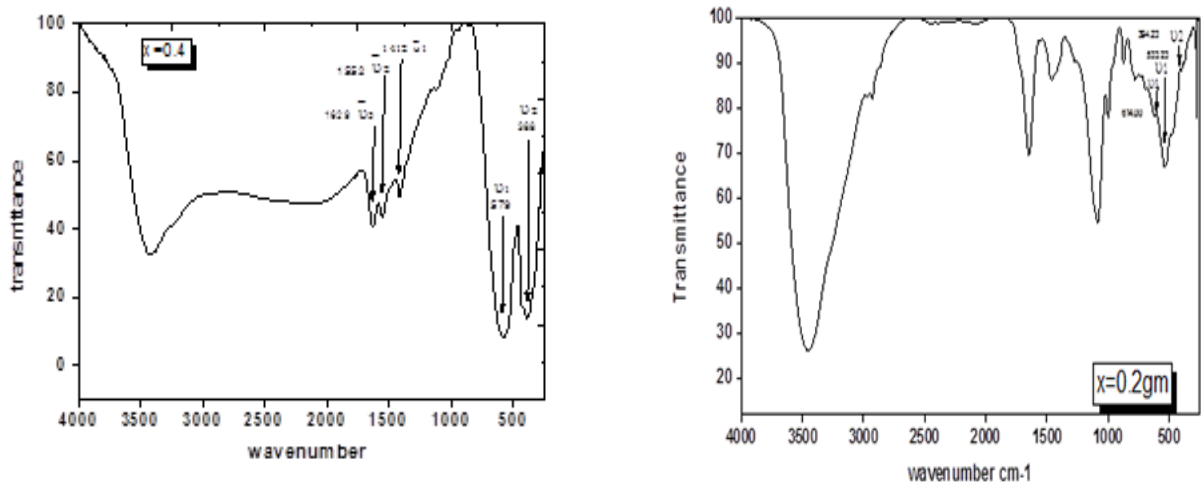


**(a)** **(b)**

**Fig. (4): FTIR spectra of (a) $Ni_{0.6}Mg_{0.4}Fe_2O_4$ and (b) $Ni_{0.6}Mg_{0.4}Fe_2O_4$ with methyl cellulose**

**Table (3): The absorption spectra of tetrahedral site ($\upsilon_1$) and octahedral site ($\upsilon_2$), the bond length $R`_A$ and Force constant for $Ni_{0.6}Mg_{0.4}Fe_2O_4$ and $Ni_{0.6}Mg_{0.4}Fe_2O_4$ with methyl cellulose**

| sample | $\nu_1$ | $\nu_2$ | $F_{tetra}$ (dyne/cm) *$10^5$ | $F_{octa}$ (dyne/cm) * $10^5$ |
|---|---|---|---|---|
| $Ni_{0.6}Mg_{0.4}Fe_2O_4$ | 579 | 388 | 2.45 | 1.10 |
| $Ni_{0.6}Mg_{0.4}Fe_2O_4$ + methyl cellulose. | 533 | 394 | 2.45 | 1.10 |

### 3.5 Thermogravimetric Analysis (TGA)

Fig. (5) displays the thermodynamic curves for $Ni_{0.6}Mg_{0.4}Fe_2O_4$ sample in the temperature zone between room temperature to 900 °C. TGA curves have two junctures owing to weight loss. 1st juncture of room temperature till 100 °C is because of $H_2O$ evaporation while the second is from 500 °C up to 800 °C that is on account of the degradation and decomposition of the organic phase that happened through the synthetization of the sample by flash auto combustion method.

Fig. (5) illustrates that MC decomposition temperature was the highest compared to cellulose, for the deformation in the MC crystal structure (by breaking the hydrogen bond). Furthermore, a slight weight loss was predestining near 150 °C because of the vaporization of lagging water from cellulose. Other weight loss that is major was monitored approximately 350 °C of MC because of the degradation of the main chain. On comparing MC and composite, the attitude was distinct, where 1st and 2nd weight losses for the composite were conveyed to rising worth, refereeing a perfect interaction among Ni Mg ferrite and MC matrix that consolidated its thermal stability. The weight loss rate jointly 400 °C and 600 °C pointed to the fact that Ni particles in Ni Mg ferrite were consolidated into the cellulose framework and shaped solid linkage bonds with higher binding energy, glass transference temperature and thermal steadiness through the fabrication procedure.

### 3.6 VSM analysis

M-H loop which show the magnetization as a function of the magnetic field for $Ni_{0.6}Mg_{0.4}$ $Fe_2O_4$ is shown in Fig.(6). The Figure shows that the material has ferrimagnetic properties with soft character. The magnetic parameters such as saturation magnetization ($M_s$), remnant magnetization ($M_r$), area of hysteresis loop, coercive field, squares and magnetic moment can be deduced from the hysteresis loop. The value of saturation magnetization, coercivity and remnant magnetization is given in Table (4). M-H loop for Ni Mg ferrite + MC signalized that the worth of Hc, Ms, and Mr are 0.4 Oe, 17.44 emu/g, and 0.28 emu/g, respectively. The worth of $M_s$ decreases by introducing MC composite as given in Table (4).

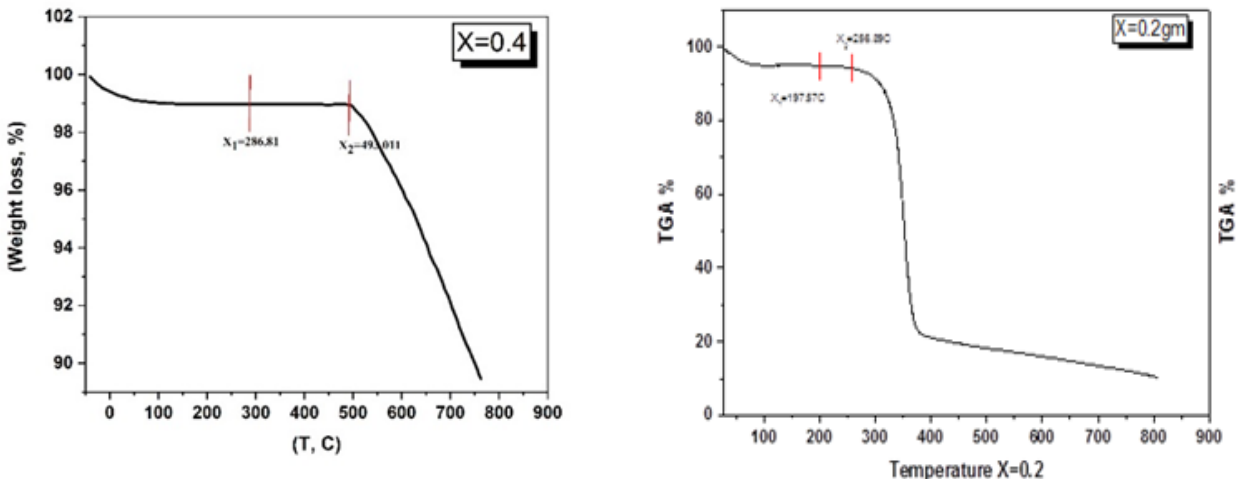


**(a)** **(b)**

**Fig. (5): TGA curves of (a) $Ni_{0.6}Mg_{0.4}Fe_2O_4$ and (b) $Ni_{0.6}Mg_{0.4}Fe_2O_4$ with methyl cellulose**

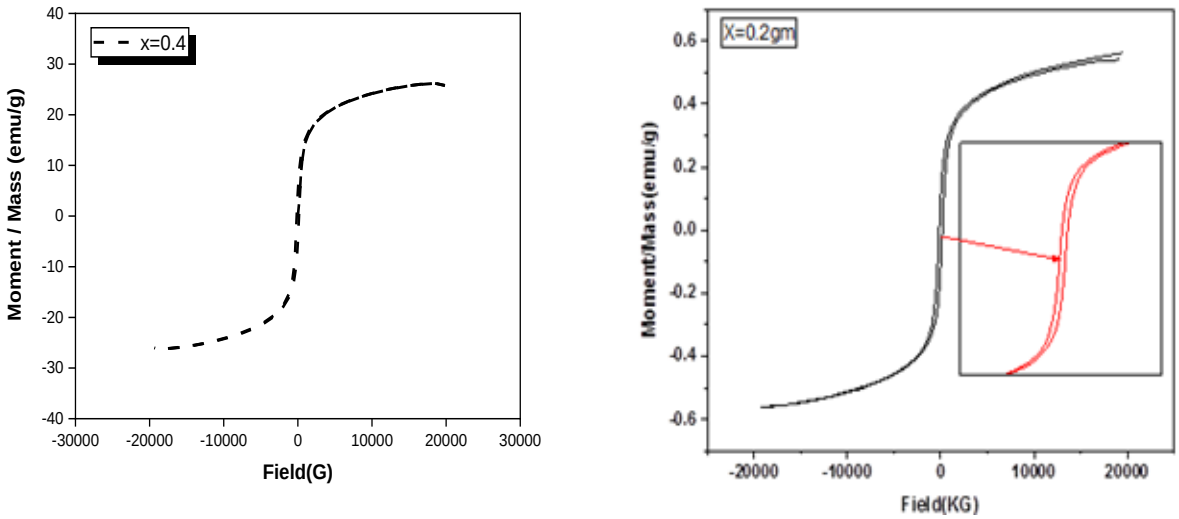


**(a)** **(b)**

**Fig. (6): Magnetic hysteresis loop for (a) $Ni_{0.6}Mg_{0.4}Fe_2O_4$ and (b) $Ni_{0.6}Mg_{0.4}Fe_2O_4$ with methyl cellulose**

**Table (4): the worth for $M_s$, $H_c$, $M_r$ and Experimental magnetic moments ($\mu_{exp}$) of $Ni_{0.6}Mg_{0.4}Fe_2O_4$ and $Ni_{0.6}Mg_{0.4}Fe_2O_4$ with methyl cellulose**

| X | $M_s$ (emu/g) | $H_c$ (G) | $M_r$ (emu/g) | $\mu_{exp}$ ($\mu_B$) |
|---|---|---|---|---|
| $Ni_{0.6}Mg_{0.4}Fe_2O_4$ | 26.207 | 147.77 | 4.9817 | 1.0352 |
| $Ni_{0.6}Mg_{0.4}Fe_2O_4$ + MC | 0.56263 | 197.08 | 0.11930 | - |

### 3.7 Magnetic Permeability:

Fig. (7) shows the variation of magnetic permeability of the studied sample at different frequencies from 1kHz to 50kHz. The permeability increases with temperature up to certain peak (Hopkinson peak) that indicates the existence of a single phase for the prepared sample. This peak occurred near the Curie temperature of the material that was determined from the Figure and tabulated in Table (5). The magnetic anisotropy constant vs. temperature is shown in Fig. (8), which has an inverse behavior of the permeability. The sudden decrease in the magnetic anisotropy occurred near Curie temperature.

The initial permeability sharply decreased at Curie temperature $T_C$ which make the studied samples very strong candidate for magnetic switch devices. A disturbed curve for NiMg ferrite + MC composite was obtained because of the non-magnetic nature of MC.

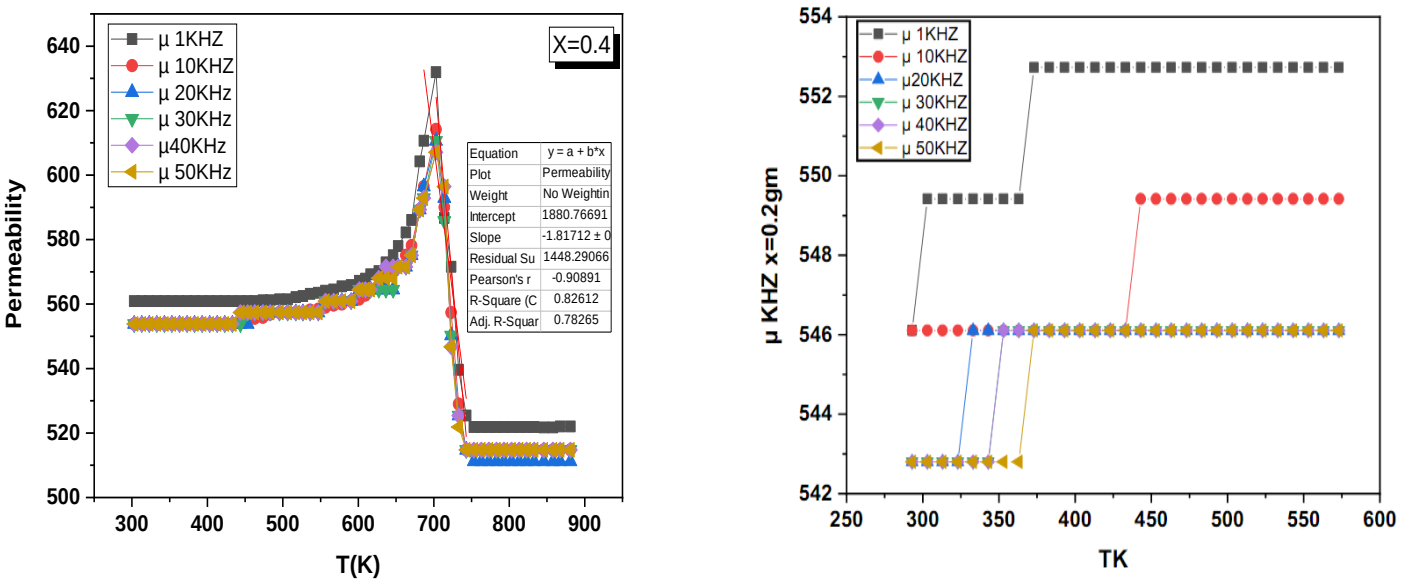


**Fig. (7): The variation of initial magnetic permeability (μi) with temperature for $Ni_{0.6}Mg_{0.4}Fe_2O_4$ at different frequencies**

**Table (5): The Curie temperature (Tc), the Magnetic anisotropy constant, Permeability ($\mu_i$), Rate of decrease of $\mu_i$ and Grain size for $Ni_{0.6}Mg_{0.4}Fe_2O_4$**

| x | Tc (K) | Magnetic anisotropy (K) | Permeability ($\mu_i$) | Rate of decrease of $\mu_i$ | Grain size (D) |
|---|---|---|---|---|---|
| 0.4 | 704.21 | 132 | 560 | 1.817 | 108.66 |

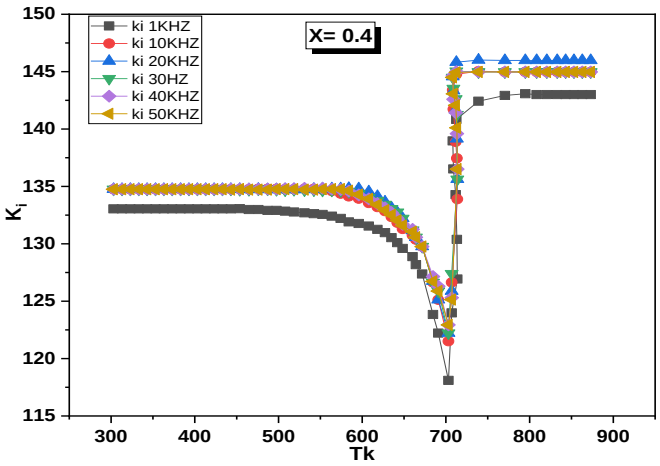


**Fig. (8): The magnetic anisotropy constant as a function of temperature for $Ni_{0.6}Mg_{0.4}Fe_2O_4$**

### 3.8 UV-Vis measurements:

Fig. (9) illustrates the UV-vis absorbance spectra of $Ni_{0.6}Mg_{0.4}$ $Fe_2O_4$ for various ferrite content (x = 0.2, 0.4, 0.6 and 0.8) grams doped in 2 grams of methyl cellulose (MC) thin films at room temperature. The UV-vis absorption spectrum displays that the absorption of $Ni_{0.6}Mg_{0.4}$ $Fe_2O_4$ at MC is in the UV-A region up to 270 nm. The absorption edge for all samples is shown in the absorption spectrum of the thin films, where the absorption edge for x = 0.2, 0.6 and 0.8 was shifted towards longer wavelengths. This increase could be because of the variation of the optical band gap that enhances the semi conducting behavior of the samples. The absorbance for x = 0.4 sample is lower than the other samples, then the absorbance increase at x = 0.6 and 0.8. Another stage of absorbance occurs in x = 0.4 sample from λ = 400 nm (visible region) to λ = 500 nm. The wavelength ranges of absorbance increase by increasing the ferrite content; these values are shown in Table (6).

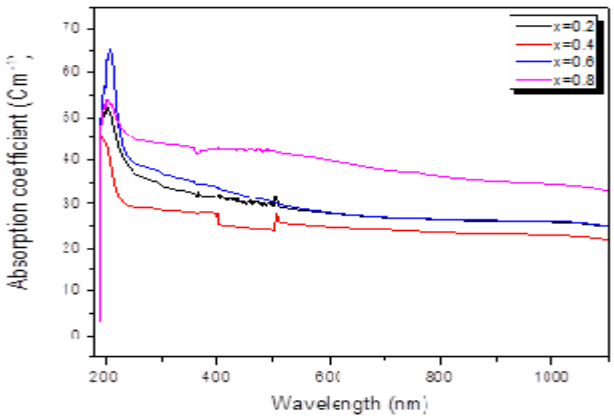


**Fig. (9): UV- visible spectroscopy in the wavelength range 190-1100 nm at room temperature for different ferrite content of $Ni_{0.6}Mg_{0.4}$ $Fe_2O_4$ in MC thin films**

**Table (6): The wavelength ranges of absorbance, refractive index (n) and urbach tail energy ($E_u$) for different ferrite content of $Ni_{0.6}Mg_{0.4}$ $Fe_2O_4$ in methyl cellulose (MC) thin films**

| Sample designation ferrite content (gm) | The wavelength ranges of absorbance (nm) | | Refractive index (n) at 650 nm | Eu (eV) |
|---|---|---|---|---|
| | From | To | | |
| x = 0.2 | 200 | 250 | 6.5 | 2.11 |
| x = 0.4 | 195 | 225 | 5.8 | 1.76 |
| x = 0.6 | 220 | 270 | 6.5 | 2.66 |
| x = 0.8 | 220 | 280 | 10 | 1.67 |

The dependence of direct and indirect optical energy band gap on the photon energy are illustrated in Fig. (10(a,b)) respectively. The direct energy band gap $E_g$ of the particles is calculated from the absorption spectra by the following formula [29,30]:

$$(\alpha h\upsilon)^2 = A(h\upsilon - E_g) \quad \textbf{(1)}$$

the direct and indirect allowed transitions may be on account of the transition energy for electrons [31].The worth of energy band gap $E_g$ increased with increasing the ferrite content to become the maximum worth at x = 0.6 and then decreased at x = 0.8. The indirect energy band gaps $E_g$ for the samples were calculated by the following equation [32, 33]:

$$(\alpha h\upsilon)^{0.5} = A(h\upsilon - E_g) \quad \textbf{(2)}$$

The indirect energy band gap $E_g$ plot displays that the energy band gap $E_g$ worth is 2.729 ev for the lowest ferrite content (x=0.2) and increases by increasing the ferrite content to get smaller again by increasing the ferrite content (at x = 0.8). Fig. (11) shows the dependence of $E_g$ values for direct and in-direct transitions on $Ni_{0.6}Mg_{0.4}$ $Fe_2O_4$ at methyl cellulose (MC) thin films content. The behavior of direct and indirect energy band gap $E_g$ is similar, as shown in Fig. (11).

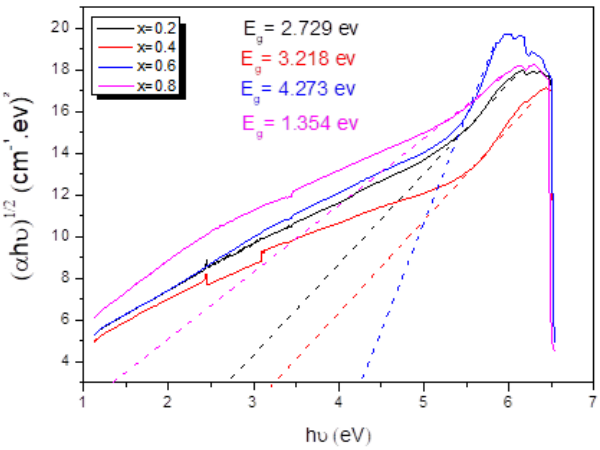


**(a)**

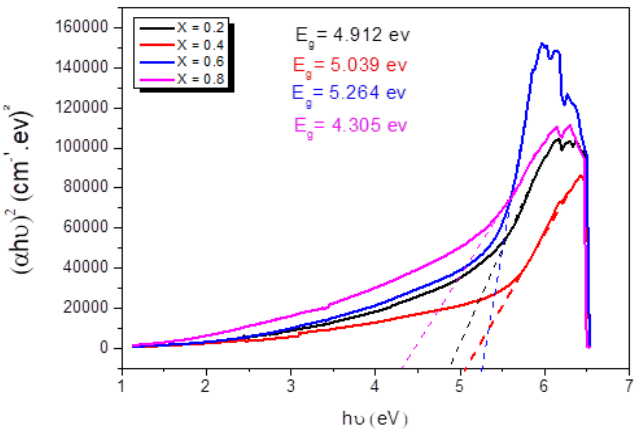


**(b)**

**Fig.10:(a) the dependence of (a) $(\alpha h\nu)^2$ on the photon energy (hν) and (b) the dependence of $(\alpha h\nu)^{1/2}$ on photon energy (hν) for different ferrite content of $Ni_{0.6}Mg_{0.4}$ $Fe_2O_4$ in methyl cellulose (MC) thin films**

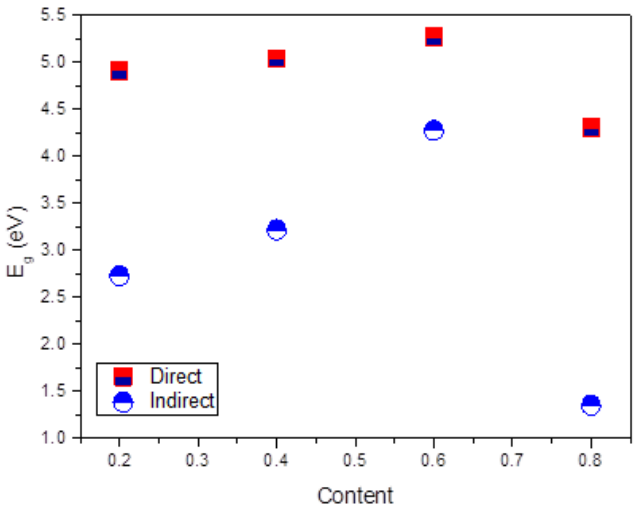


**Fig. (11): The dependence of $E_g$ values for direct and indirect transitions on $Ni_{0.6}Mg_{0.4}$ $Fe_2O_4$ in methyl cellulose (MC) thin films**

$E_u$ "Urbach tail energy" is a gauge of the flaw levels and the beget localized cases in the prohibitive band gap and could be calculated by the following equation [34, 35]:

$$\alpha(\upsilon) = \alpha_o e^{(h\upsilon/E_u)} \qquad \textbf{(3)}$$

Where, $\alpha_o$ and $\alpha$ ($\upsilon$) are a constant and the absorption coefficient, respectively that could be assessed by utilizing the relation of Beer–Lambert [36, 37]:

$$\alpha(\upsilon) = 2.303\,(\frac{A}{L}) \qquad \textbf{(4)}$$

Where, L is the sample thickness and A is the absorbance and is determined by log ($I_0$/ I) where $I_0$ is the incident intensity and I is transmitted light.

The variation of ln ($\alpha$) versus ($h\upsilon$) as presented in Fig. (12) and the $E_u$ worth was determined by the reciprocal of the slopes and recorded in Table (6). $E_u$ has the maximum worth for x = 0.6 where it is equal to 2.66 eV the lowest value of $E_u$ for x = 0.8 where it is equal to 1.67. The disorders of the structure in films occurred as observed from urbch tail energy analysis. The variation in the optical energy band gap ($E_g$) and urbach tail energy ($E_u$) by adding ferrite content in polymer thin films may be because of the increase in the grain size.

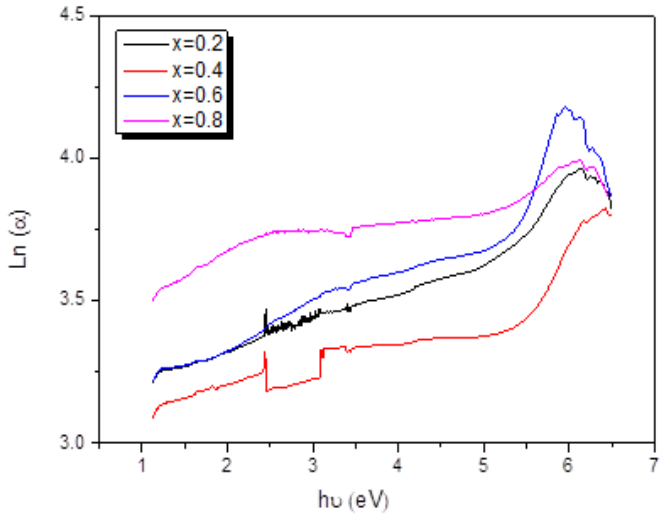


**Fig. (12): Variation of ln($\alpha$) versus ($h\nu$) for different ferrite content of $Ni_{0.6}Mg_{0.4}$ $Fe_2O_4$ in methyl cellulose (MC) thin films**

Fig. (13) displays the dependence of the refractive index (n) of $Ni_{0.6}Mg_{0.4}$ $Fe_2O_4$ at methyl cellulose (MC) thin films on wavelength $\lambda$. The refractive index value is estimated at the wavelength 650 nm and recorded in Table (6). The refractive index values appear rather large, ranging from 5.8 to 10. The maximum value of the refractive index is 10 for the largest content of ferrite (x = 0.8), where the lowest value is seen for sample x = 0.4 of the ferrite content. The increase of the refractive index (*n)* values assured the enhancement of packing density of the polymer (MC) with rising the ferrite content in the films. The refractive index (n) result shows that the decrease of inter-atomic spacing on account of the packing density of the material get enhanced with the addition of the ferrite content.

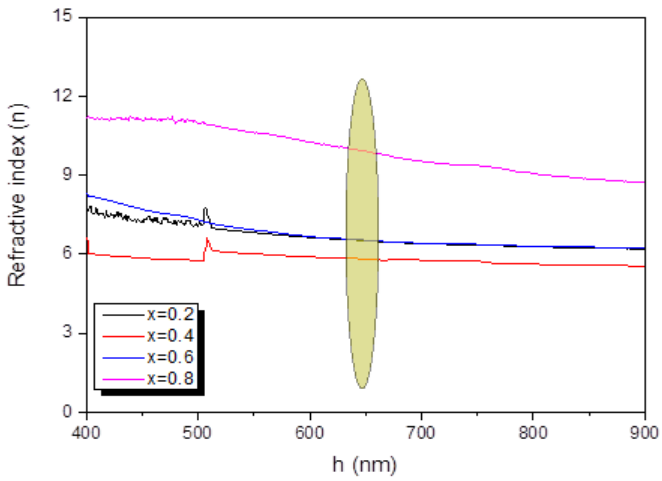


**Fig. (13): The calculated refractive index of the different ferrite content of $Ni_{0.6}Mg_{0.4}$ $Fe_2O_4$ in methyl cellulose (MC) thin films**

The optical conductivity (σ) of $Ni_{0.6}Mg_{0.4}$ $Fe_2O_4$ at methyl cellulose (MC) thin films dependent on the photon energy hυ (ev) is shown in Fig. (14). The optical conductivity calculated utilizing the refractive index (n) and the absorption coefficient (α) results using the next equation [38]:

$$\sigma = \frac{\alpha n C}{4\pi} \qquad (5)$$

Where, C is the velocity of light in the space. For all samples, the optical conductivity increased by increasing the photon energy until the photon energy edge the increasing became sharply. The conductivity value of the sample 0.8 is greater than that of the other samples. The increase in the optical conductivity is related to the increase of the charge carrier's concentration by adding ferrite content.

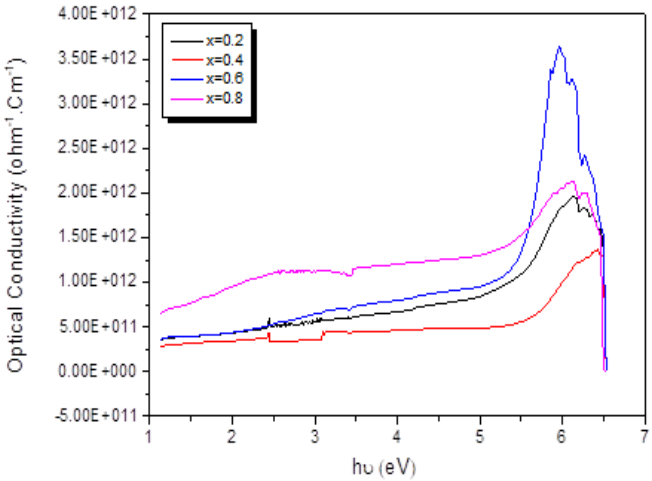


**Fig. (14): The calculated ($\sigma_{optical}$) as a function of (hυ) for different ferrite content of $Ni_{0.6}Mg_{0.4}$ $Fe_2O_4$ in methyl cellulose (MC) thin films**

## 4. CONCLUSION

$NiMgFe_2O_4$ nanoparticles and polymer nanocomposites based on methyl cellulose (MC) with $NiMgFe_2O_4$ nanoferrite has been debated. From XRD, the observed broad refection peaks of alkali cellulose may be attributed to the interaction of NiMg ferritee particles with MC. The micro images suggest that the ferrite nanoparticles were successfully supported on the MC. The composite surface consists of cylindrical fibers with steady ferrite grains strewn through MC fibers implicating several vacants indicating the composite's high porosity and resistivity. A major weight loss was monitored and found to be approximately 350 °C of MC because of the degradation of the main chain. The value of $M_s$ decreases by introducing MC composite from M-H loop. The urbach tail energy $E_u$ has the maximum value for x = 0.6 where it is equal to 2.66 eV, the lowest value of $E_u$ for x = 0.8 where it is equal to 1.67.

## REFERENCES

[1] T. Kamal, Y. Anwar, S.B. Khan, M.T.S. Chani, A.M. Asiri, Dye adsorption and bacteri- cidal properties of TiO2/chitosan coating layer, Carbohydr. Polym. 148 (2016)153–160.

[2] T. Kamal, M. Ul-Islam, S.B. Khan, A.M. Asiri, Adsorption and photocatalyst assisted dye removal and bactericidal performance of ZnO/chitosan coating layer, Int. J. Biol. Macromol. 81 (2015) 584–590.

[3] S.B. Khan, F. Ali, T. Kamal, Y. Anwar, A.M. Asiri, J. Seo, CuO embedded chitosan spheres as antibacterial adsorbent for dyes, Int. J. Biol. Macromol. 88 (2016) 113–119.

[4] S.A. Khan, S.B. Khan, T. Kamal, M. Yasir, A.M. Asiri, Antibacterial nanocomposites based on chitosan/Co-MCM as a selective and efficient adsorbent for organic dyes, Int. J. Biol. Macromol. 91 (2016) 744–751.

[5] I. Ahmad, S.B. Khan, T. Kamal, A.M. Asiri, Visible light activated degradation of organic pollutants using zinc–iron selenide, J. Mol. Liq. 229 (2017) 429–435.

[6] S.B. Khan, S.A. Khan, M. Marwani Hadi, E.M. Bakhsh, Y. Anwar, T. Kamal, et al., Anti- bacterial PES-cellulose composite spheres: dual character toward extraction and catalytic reduction of nitrophenol, RSC Adv. 6 (2016) 110077–110090.

[7] T. Benhalima, H. Ferfera-Harrar, Eco-friendly porous carboxymethyl cellulose/dextran sulfate composite beads as reusable and efficient adsorbents of cationic dye methylene blue, Int. J. Biol. Macromol. 132 (2019) 126–141.

[8] Z. Li, W. Wu, W. Jiang, L. Zhang, Y. Li, Y. Tan, et al., Preparation and regeneration of a thermo-sensitive adsorbent material: methyl cellulose/calcium alginate beads (MC/CABs), Polym. Bull. 77 (2020) 1707–1728, https://doi.org/10.1007/s00289-019-02808-w.

[9] F. Tamaddon, A. Nasiri, G. Yazdanpanah, Photocatalytic degradation of ciprofloxacin using CuFe2O4@methyl cellulose based magnetic nanobiocomposite, MethodsX 7 (2020) 74–81, https://doi.org/10.1016/j.mex.2019.12.005100764.

[10] A. Nasiri, F. Tamaddon, M.H. Mosslemin, M. Faraji, A microwave assisted method to synthesize nanoCoFe2O4@methyl cellulose as a novel metal-organic framework for antibiotic degradation, MethodsX 6 (2019) 1557–1563.

[11] A. Nasiri, F. Tamaddon, M.H. Mosslemin, M.A. Gharaghani, A. Asadipour, New mag- netic nanobiocomposite CoFe2O4@methylcellulose: facile synthesis, characteriza- tion, and photocatalytic degradation of metronidazole, J. Mater. Sci. Mater. Electron. 30 (2019) 8595–8610.

[12] L. Zhang, Y.Q. Lu, Y.L. Peng, Y.X. Yu, Y. Zhao, Y. Ma, et al., Microstructures and properties of photophobic films composed of hydroxypropyl methylcellulose and differ- ent salts, Int. J. Biol. Macromol. 120 (2018) 945–951.

[13] N. Fiol, M.G. Vásquez, M. Pereira, Q. Tarrés, P. Mutjé, M. Delgado-Aguilar, TEMPO- oxidized cellulose nanofibers as potential Cu(II) adsorbent for wastewater treat- ment, Cellulose 26 (2019) 903–916.

[14] Shuhaimi, N.E.A.; Teo, L.P.; Majid, S.R.; Arof, A.K. Transport studies of $NH_4$ $NO_3$ doped methyl cellulose electrolyte. Synth. Met. **2010**, 160, 1040–1044. [CrossRef]

[15] Li, S.; Lin, M.M.; Toprak, M.S.; Kim, D.K.; Muhammed, M. Nanocomposites of polymer and inorganic nanoparticles for optical and magnetic applications. Nano Rev. **2010**, 1, 5214. [CrossRef] [PubMed]

[16] Yashar, A.; Uumut, A.; Emsettin, T. Dielectric and Optical Properties of CdS–Polymer Nanocomposites Prepared by the Successive Ionic Layer Adsorption and Reaction (SILAR). J. Electron. Mater. **2014**, 43, 1226–1231.

[17] Tiwari, A.; Khan, S.A.; Kher, R.S.; Dhobled, S.J.; Chandel, A.L.S. Synthesis, characterization and optical properties of polymer-based ZnSnanocomposites. Luminescence **2016**, 31, 428–432. [CrossRef] [PubMed]

[18] Bockstaller, M.R.; Thomas, E.L. Optical Properties of Polymer-Based Photonic Nanocomposite Materials. J. Phys. Chem. B **2003**, 107, 10017–10024. [CrossRef]

[19] Wu, Y.; Wadia, C.; Ma, W.; Sadtler, B.; Alivisatos, A.P. Synthesis and Photovoltaic Application of Copper (I) Sulfide Nanocrystals. Nano Lett. **2008**, 8, 2551–2555. [CrossRef] [PubMed]

[20] Shunichiro, I.; Amane, H.; Madoka, Y.; Kazuo, T.; Yoshiki, C. Synthesis of Aggregation-Induced Emission-Active Conjugated Polymers Composed of Group 13 Diiminate Complexes with Tunable Energy Levels via Alteration of Central Element. Polymers **2017**, 9, 68. [CrossRef]

[21] Tanwistha, G.; Jayanthy, S.P.; Vijayakumar, C.N. Self-Assembled Organic Materials for Photovoltaic Application. Polymers **2017**, 9, 112. [CrossRef]

[22] Mozer, A.J.; Sariciftci, N.S. Conjugated polymer photovoltaic devices and materials. C.R. Chimie **2006**, 9, 568–577. [CrossRef]

[23] Mallajosyula, A.T.; Srivastava, N.; Kumar, S.S.; Mazhari, B. Characterization of matrix and isolated organic solar cells. Sol. Energy Mater. Sol. Cells **2010**, 94, 1319–1323. [CrossRef]

[24] O.M Hemeda, A. Tawfik, M. Mostafa, M. Zaki, M.I. Abd EL Ati, IOP Conf. Series: Journal of Physics: Conf. Series **1253** (2019) 012026.

[25] J. Chen, M.C. Che and F. Yan, Advances in Applied Ceramics, 114:6, 2015, 344-349.

[26] M.N. Akhtar , M.A. Khan , M. Ahmad , M.S. Nazir , M. Imran , A. Ali, A. Sattar , G. Murtaza , Journal of Magnetism and Magnetic Materials, 421 (2017) 260-268.

[27] H. Moradmard, S. Farjami, P. Tphidi, Z. Abbas, M. Khaleghi, Journal of Alloys and Compounds, 650 (2015)116-122.

[28] O.M Hemeda, B.I. Salem, M. Mostafa, The European Physical Journal Plus, (2020) 135:46.

[29] Henaish A M A and Abouhaswa A S 2020 *Bull. Mater. Sci*. **43** 149

[30] Lee C S, Matori K A, Ab Aziz S H, Mohamed Kamari H, Ismail I and Mohd Zaid M H 2017 *Optik (Stuttg)*. **136** 129.

[31] M.M. Abutalib a, A. Rajeh b, Polymer Testing 91 (2020) 106803

[32] Lakshmanaperumal S, Hemalatha P, Alagar M and Navaneethapandiyaraj K 2015 *IJCPS* **4** 1.

[33] Kripal R, Gupta A K, Srivastava R K and Mishra S K 2011 *Spectrochim. Acta - Part A Mol. Biomol. Spectrosc*. **79** 1605.

[34] R.P. Chahal, S. Mahendia, A. Tomar, S. Kumar, Journal of Alloys and Compounds, 538 (2012) 212-219.

[35] M.A. Morsi, A.M. Abdelghany, Materials Chemistry and Physics 201(2017)100-112.

[36] E. Abdelrazek, I. Elashmawi, A. El-Khodary, A. Yassin, Current Applied Physics, 10 (2010) 607-613.

[37] A. Abdelghany, E. Abdelrazek, D. Rashad, Spectrochimica Acta Part A: Molecular and Biomolecular Spectroscopy, 130 (2014) 302-308.

[38] A. M. A. Henaish, A. N. El-Sharkawy, S. A. Shama, O. M. Hemeda, and R. Ghazy, J. Phys. Conf. Ser. **1253**, (2019). https://doi.org/10.1088/1742-6596/1253/1/012024.